Journal of Materials Chemistry A

ROYAL SOCIETY OF CHEMISTRY

PAPER

View Article Online
View Journal | View Issue

Cite this: J. Mater. Chem. A, 2020, 8, 15746

Ultrathin RuRh@(RuRh)O_2 core@shell nanosheets as stable oxygen evolution electrocatalysts†

Kai Wang, ‡[a] Bolong Huang,‡[b] Weiyu Zhang,[a] Fan Lv,[a] Yi Xing,[a] Wenshu Zhang,[a] Jinhui Zhou,[a] Wenxiu Yang,[a] Fangxu Lin,[a] Peng Zhou,[a] Mingqiang Li,[c] Peng Gao [cd] and Shaojun Guo *[ae]

The oxygen evolution reaction (OER) is of prime importance in the development of highly efficient electrochemical energy conversion and storage technologies such as water splitting and zinc air batteries. Ru-based nanocatalysts are still the best catalytic system for the OER; however, one of the greatest challenges is their relatively poor stability for the OER. Here, we report a novel architecture of ultrathin RuRh@(RuRh)O_2 core/shell nanosheets with a core of ultrathin metallic RuRh nanosheets and a shell of RuO_2/RhO_2 oxides as superb electrocatalysts toward the OER. The RuRh@(RuRh)O_2 core/shell nanosheets can achieve a high electrocatalytic activity toward the OER, with a low 245 mV overpotential at 10 mA cm^{-2} and a Tafel slope of 51.2 mV dec^{-1}, better than most state-of-the-art Ru-based or Ir-based electrocatalysts for the OER. Moreover, the RuO_2/RhO_2 oxides shell protect the normally labile RuRh NSs core against dissolution during the OER process, revealed by detailed rotating ring disk electrode (RRDE) measurements for simultaneously recording the dissolution of Ru on the ring electrode and the *ex situ* measurement of Ru dissolution using the galvanostatic method. Therefore, the RuRh@(RuRh)O_2 core/shell nanosheets exhibit much better OER stability in acid media compared with RuRh nanosheets and commercial RuO_2. Theoretical calculations reveal that once the formation of the surface oxidation layers is achieved, the O-sites evidentially crossover the Fermi level which could guarantee the high electroactivity towards adsorbates while the RuRh core serves as an electron reservoir with high electrical conductivity. The synergistic effect between the core and shell structure leads to the superior OER performance.

Received 22nd March 2020
Accepted 22nd May 2020

DOI: 10.1039/d0ta03213a

rsc.li/materials-a

Introduction

Electrocatalytic splitting of water into molecular hydrogen and oxygen using polymer electrolyte membrane (PEM) electrolyzer architectures plays a critical role in the conversion of renewable electrical energy into fuels.[1–3] The splitting of water involves two related electrochemical reactions in an electrolyzer, with an anodic oxygen evolution reaction (OER) and a cathodic hydrogen evolution reaction (HER). Compared with the two-electron HER proceeding at the cathode, the anodic OER is the bottleneck in this process due to the sluggish kinetics of multiple-proton-coupled electron transfer at high oxidative potential, and hence dominates the large overpotential of whole overall water electrolysis devices.[4–6] Therefore, the search for OER electrocatalysts with high intrinsic activity and preferable stability, especially in acid media, remains an outstanding problem so far.[7] Ruthenium and its oxides have been proved to be the most active oxygen evolution reaction (OER) catalysts.[8] However, despite its highest activity,[8,9] metallic Ru would deactivate very fast during the OER in acid media due to the fast dissolution of oxidized Ru species,[10,11] and the dissolution rate of Ru is 2–3 orders of magnitude higher than that of its respective oxides.[12] In contrast, Rh is more stable than Ru during the OER in an acidic environment and the dissolution rate of Rh is merely one percent of the Ru dissolution rate.[13a] Therefore, it is of significant importance to design RuRh-based nanostructures that enhance the stability without sacrificing their high activity;[13b] however, achieving such a target is still a grand challenge.

Herein, we propose a method to design ultrathin RuRh@(RuRh)O_2 core/shell nanosheets consisting of ultrathin metallic RuRh nanosheets as the core and a few layers of (RuRh)O_2 oxides as the shell. The RuRh@(RuRh)O_2 core/shell nanosheets

[a]Department of Materials Science and Engineering, College of Engineering, Peking University, Beijing 100871, China. E-mail: guosj@pku.edu.cn
[b]Department of Applied Biology and Chemical Technology, The Hong Kong Polytechnic University, Hung Hom, Kowloon, Hong Kong SAR, 999077, China
[c]Electron Microscopy Laboratory, International Center for Quantum Materials School of Physics Peking University, Beijing 100871, China
[d]Collaborative Innovation Center of Quantum Matter, Beijing 100871, China
[e]BIC-ESAT, College of Engineering, Peking University, Beijing 100871, China

† Electronic supplementary information (ESI) available. See DOI: 10.1039/d0ta03213a

‡ Kai Wang and Bolong Huang contributed equally to this work.

have superb electrocatalytic activity toward the OER, with a low 245 mV overpotential at 10 mA cm^{-2} and a Tafel slope of 51.2 mV dec^{-1}, better than most state-of-the-art Ru-based or Ir-based electrocatalysts for the OER. Besides, ultrathin RuRh@$(RuRh)O_2$ core@shell nanosheets exhibit much better OER stability and faradaic efficiency than RuRh NSs because the covering layer of the $(RuRh)O_2$ oxides shell can prevent the fast Ru dissolution of the metallic RuRh NSs core during the OER, which is revealed by the RRDE measurements for simultaneously recording the dissolution of Ru on the ring electrode and the *ex situ* measurement of Ru dissolution using the galvanostatic method. DFT systematically investigates the electronic modulations induced by the oxidation surface to the electroactivity of the core@shell RuRh@$(RuRh)O_2$. Both electronic and energy calculations indicate that the boosting effect on OER performance originates from the highly electroactive oxidation layer, supporting the experimental observations.

Results and discussion

Ultrathin RuRh@$(RuRh)O_2$ core/shell nanosheets were synthesized *via* a two-step method. Firstly, ultrathin RuRh nanosheets (RuRh NSs) were synthesized by a colloidal-chemical approach.[14a] Then, the ultrathin RuRh nanosheets were loaded on carbon black (denoted as RuRh NSs/C) and annealed in air at 286 °C for 2 h to obtain the ultrathin RuRh@$(RuRh)O_2$ core@shell nanosheets supported on carbon (denoted as RuRh@$(RuRh)O_2$ NSs/C). Transmission electron microscopy (TEM) and high-resolution transmission electron microscopy (HRTEM) were conducted to investigate the morphology and structure of the as-obtained products. As shown in Fig. 1a and b, triangle nanosheets with an edge length of 16.3 ± 3.5 nm and a thickness of 1.9 ± 0.5 nm (six to eight atomic layers, Fig. S1†) were the dominant products. The Ru/Rh composition was 85/15 (Ru/Rh), determined from the TEM energy-dispersive X-ray spectroscopy (TEM-EDX) results (Fig. S2†). The powder X-ray diffraction (PXRD) pattern of the RuRh nanosheets shows that they are highly crystalline with the hexagonal close-packed (hcp) phase of Ru ($P6_3/mmc$) crystals [JCPDS 06-0663] (Fig. S3†).[14b] The HRTEM and selected-area electron diffraction (SAED) images (Fig. 1c) as well as the STEM-EELS elemental mapping results[14a] indicate that the triangle nanosheets are single-crystalline and Ru/Rh atoms are distributed randomly and uniformly across the whole nanosheets, with the regular hcp structure that extends along the *c*-axis.

After being annealed in air at a phase transition temperature of 286 °C (Fig. S4†) for 2 h, RuRh NSs/C (Fig. S5†) still maintains the 2D morphology (Fig. S6†). The PXRD result reveals that diffraction peaks of tetragonal RuO_2 ($P4_2/mnm$) crystals [JCPDS 40-1290][15] and tetragonal RhO_2 ($P4_2/mnm$) crystals [JCPDS 43-

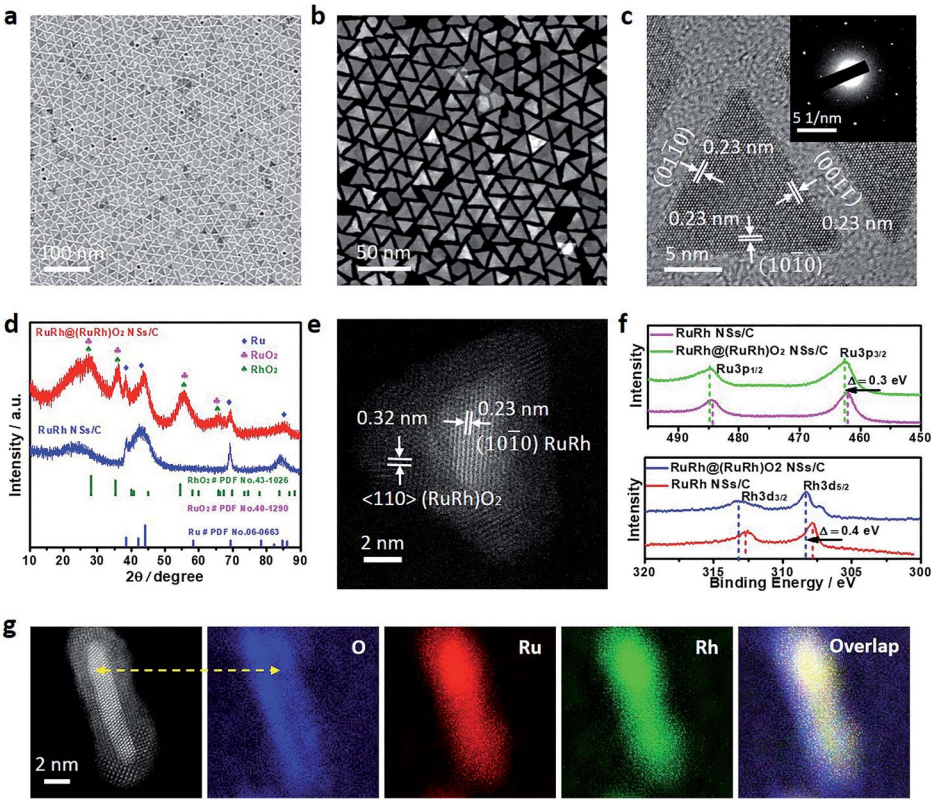

Fig. 1 Morphological and structural characterization of ultrathin RuRh NSs and RuRh@$(RuRh)O_2$ NSs. Representative (a) TEM image and (b) HAADF-STEM image of ultrathin RuRh NSs. (c) HRTEM TEM image of ultrathin RuRh NSs (the inset shows the related SAED image). (d) PXRD patterns and (e) HAADF-STEM image of the RuRh@$(RuRh)O_2$ NSs. (f) XPS analysis of Rh 3d and Ru 3p spectra. (g) STEM-EDX elemental mapping of the RuRh@$(RuRh)O_2$ NSs.

1026][16] appear (Fig. 1d). The HAADF-STEM image (Fig. 1e and S7†) shows that the annealed RuRh NSs are transformed to a core/shell structure, with the RuRh NSs inside as the core and the $(RuRhO)_2$ outside as the shell. X-ray photoelectron spectroscopy (XPS) was used to study the ratio of Ru/Rh in both the core and the shell and the chemical states of Ru and Rh after the annealing process. All the binding energies were calibrated to C 1s carbon at 284.8 eV (Fig. S8†) to eliminate differences in sample charging.[17] The survey spectra of RuRh NSs and RuRh@$(RuRh)O_2$ NSs (Fig. S9†) indicate that the ratio of Ru/Rh in both the core and the shell is basically the same, 85/15, which is in accordance with the EDS results. Besides, as shown in Fig. 1e, the XPS of the RuRh@$(RuRh)O_2$ NSs in the Ru 3p region and Rh 3d region shows an obvious positive shift of 0.3–0.4 eV compared with those of the RuRh NSs, and the O 1s spectrum (Fig. S10†) shows significant metal oxide bonds after thermal treatment, indicating that the RuRh@$(RuRh)O_2$ NSs exhibit a higher valence state of oxidized species than the RuRh NSs due to the surface oxidation by thermal annealing.[18] The elemental distribution of the core@shell structure was characterized by aberration-corrected STEM-EDX (Fig. 1g), showing that Ru and Rh are distributed uniformly in the RuRh@$(RuRh)O_2$ NSs while the oxygen signals are more abundant for the shell compared with those of the core, further verifying the formation of the core@shell structure after the annealing process.

The OER activity of the RuRh NSs, RuRh@$(RuRh)O_2$ NSs and commercial RuO_2 was studied using the rotating disk electrode (RDE) technique in O_2-saturated 0.1 M perchloric acid solution. Before the electrochemical activity test, the catalysts were activated and preoxidized through potential cycles between 0.1 V and 1.4 V *versus* RHE in N_2-saturated solution to obtain stable cyclic voltammetry curves and to avoid the disturbance of metal oxidation processes.[19] As shown in Fig. 2a, the RuRh NSs exhibit poor OER stability with fast activity fading for just a few cycles, implying that the metallic RuRh NSs are not suitable for OER catalysis despite their high activity. In contrast, the RuRh@$(RuRh)O_2$ NSs are much more stable than the RuRh NSs (Fig. 2b). The linear sweep voltammetry (LSV) curves of all the catalysts normalized to the geometrical area of the electrode with *iR* correction are shown in Fig. 2c. It can be seen that the activity decreases in the order RuRh NSs > RuRh@$(RuRh)O_2$ NSs ≫ commercial RuO_2, revealing that the RuRh NSs exhibit the high OER activity whereas the RuRh@$(RuRh)O_2$ NSs retain the high activity after the annealing process. The overpotentials of RuRh NSs, RuRh@$(RuRh)O_2$ NSs and commercial RuO_2 at 10 mA cm^{-2} are 213 mV, 245 mV and 314 mV (Fig. 2d). The corresponding Tafel slopes (Fig. S11†) are 49.3 mV dec^{-1}, 51.2 mV dec^{-1} and 110.3 mV dec^{-1}, respectively, indicating the favorable reaction kinetics of RuRh NSs and RuRh@$(RuRh)O_2$ NSs. The OER current densities converted into platinum group metal (PGM) mass-based activities (units of A g_{PGM}^{-1}) of the catalysts are shown in Fig. S12.† The mass activities of RuRh NSs and RuRh@$(RuRh)O_2$ NSs at an overpotential of 250 mV are 437.4 A g_{PGM}^{-1} and 119.8 A g_{PGM}^{-1}, which are 16.6 and 4.6 times higher than that of commercial RuO_2, respectively. Compared with most state-of-the-art Ru-based or Ir-based electrocatalysts for the OER, the RuRh@$(RuRh)O_2$ NSs have low overpotential and favorable reaction kinetics (Table S1†).

The catalytic stability of OER catalysts especially in an acid electrolyte still remains a critical issue due to the corrosive conditions under which OER catalysts operate.[20,21] As mentioned above, the RuRh NSs exhibit poor OER stability with fast fading for just a few cycles while the RuRh@$(RuRh)O_2$ NSs are more stable than the RuRh NSs. The rotating ring disk electrode (RRDE) method was used to clarify the fast fading of RuRh NSs. In the RRDE experiment, employed in a"collection

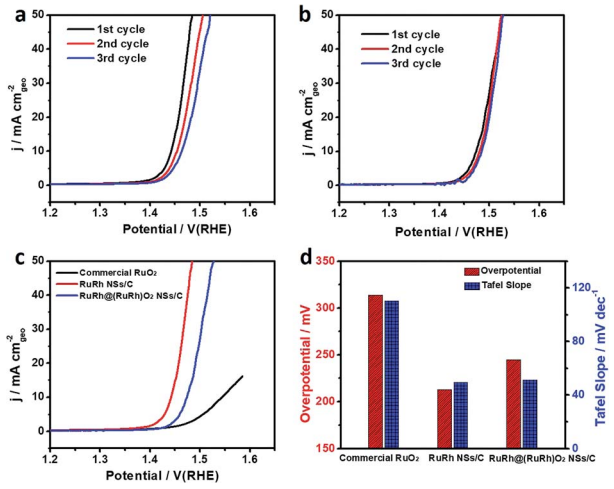

Fig. 2 Electrochemical performance of RuO_2, RuRh NSs and RuRh@$(RuRh)O_2$ NSs in O_2-saturated 0.1 M $HClO_4$. LSV curves of the (a) the RuRh NSs and (b) RuRh@$(RuRh)O_2$ NSs in 0.1 M $HClO_4$ at 1600 rpm with the scan rate 10 mV s^{-1} for the first few cycles. (c) LSV curves of the first cycle, (d) overpotentials at 10 mA cm^{-2} and Tafel slopes of RuO_2, RuRh NSs and RuRh@$(RuRh)O_2$.

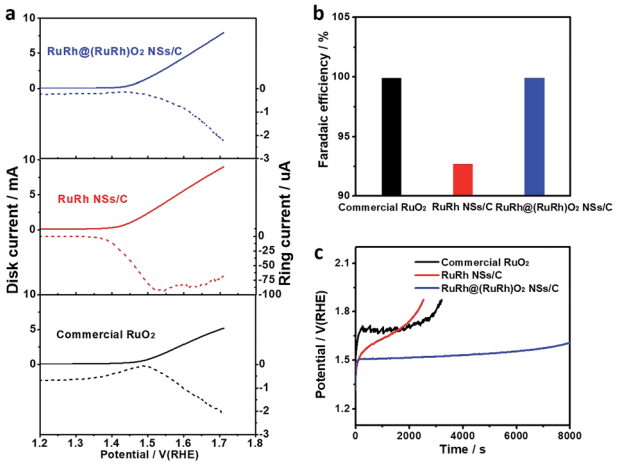

Fig. 3 OER stability of commercial RuO_2, RuRh NSs and RuRh@$(RuRh)O_2$ NSs. (a) Rotating ring disk electrode (RRDE) measurements in O_2-saturated 0.1 M $HClO_4$ for simultaneously recording the OER on the central disk electrode and the dissolution of Ru on the ring electrode (E_{ring} = 0.9 V) and (b) faradaic efficiency of the OER at 1.53 V. (c) Chronopotentiometry tests of the catalysts in 0.1 M $HClO_4$ at 5 mA cm^{-2}.

mode", the ring electrode is held at a constant potential at which Ru cations dissolved from disk electrodes in the solution phase should deposit onto the ring electrode while simultaneously recording the OER on the central Ru disk electrode.[22] As shown in Fig. 3a, the onset of Ru dissolution is accompanied by the onset of the OER, and the disk current of RuRh NSs at 1.53 V is about 92 μA, 224 times higher than that of RuRh@(RuRh)O_2 NSs, indicating that the RuRh@(RuRh)O_2 NSs are much more stable than the metallic RuRh NSs during the OER process due to much less Ru dissolution, attributed to the oxidation of RuRh to low-index rutile structured RuO_2/RhO_2.[23] The RRDE result analysis (Table S2†) further indicates that the contribution of the current corresponding to Ru dissolution relative to the total anodic current measured on the disk electrodes is only 0.049% for RuRh@(RuRh)O_2 NSs and 7.3% for RuRh NSs, implying that the faradaic efficiency of the OER for RuRh@(RuRh)O_2 NSs (approximately 99.9%) is much higher than that for RuRh NSs (92.7%) (Fig. 3b).

The stability was further evaluated by chronopotentiometry at a constant current of 5 mA cm^{-2} (Fig. 3c). The results indicate that the RuRh@(RuRh)O_2 NSs are much more stable than RuRh NSs. The amount of dissolved Ru in the electrolyte during the OER is measured by coupled plasma mass spectrometry (ICP-MS), and the results are shown in Table S3.† The Ru dissolution rate of RuRh NSs is 4.0 ng cm^{-2} s^{-1}, 66.7 times higher than that of RuRh@(RuRh)O_2 NSs (0.060 ng cm^{-2} s^{-1}), indicating that the shell structure of RuO_2/RhO_2 can protect the core of metallic RuRh NSs from dissolving during the OER process,

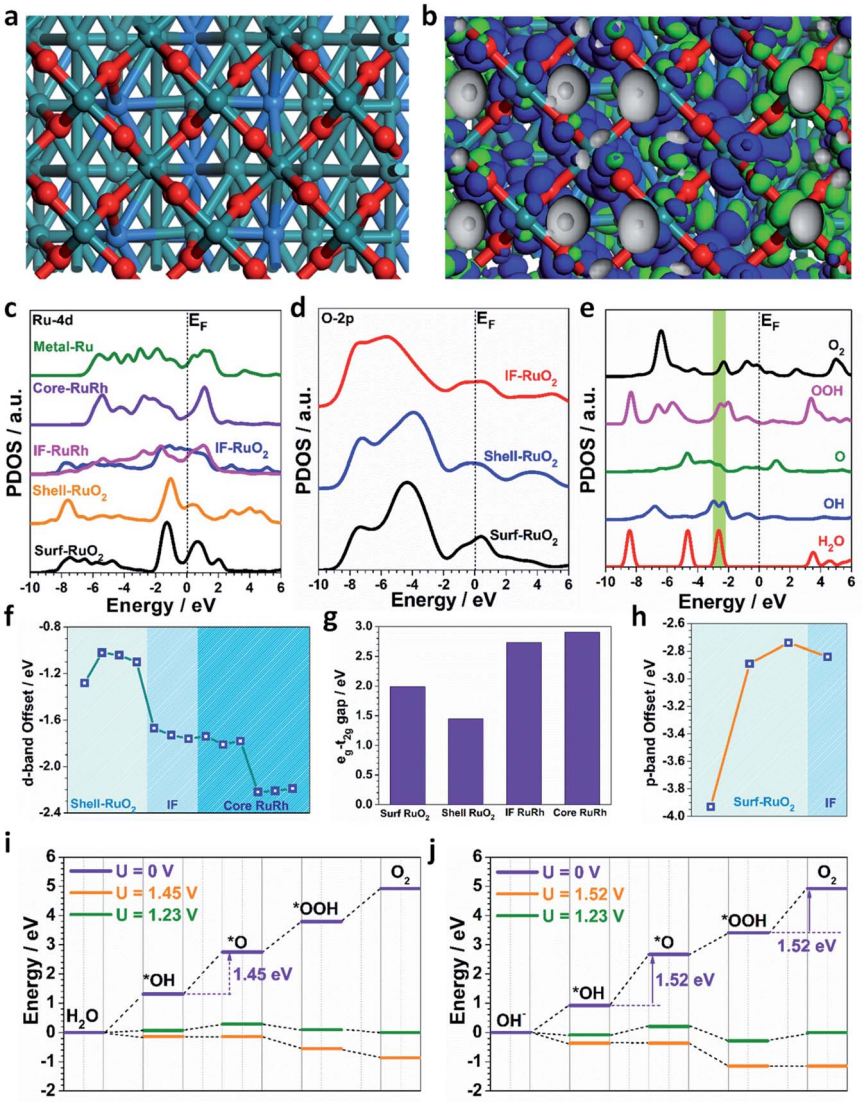

Fig. 4 Electronic properties, structural configurations and energy pathway of RuRh@(RuRh)O_2 for the OER. (a) Top view of the core–shell RuRh@(RuRh)O_2 structure. Blue balls = Rh; cyan balls = Ru; red balls = O. (b) The real spatial contour plots for bonding and anti-bonding orbitals near E_F of RuRh@(RuRh)O_2. (c) The site-dependent PDOS comparison of Ru-4d and Rh-4d in RuRh@(RuRh)O_2. (d) The site-dependent PDOS comparison of O-2p in RuRh@(RuRh)O_2. (e) The PDOS of key intermediates of the OER. (f) The d-band offset of Ru-4d in RuRh@(RuRh)O_2. (g) The site-dependent e_g–t_{2g} gap in RuRh@(RuRh)O_2. (h) The p-band offset of Ru-4d in RuRh@(RuRh)O_2. (i) Energy pathway of the OER under the acidic conditions. (j) Energy pathway of the OER under the alkaline conditions.

which is in accordance with the RRDE results. Hence, the RuRh@(RuRh)O_2 NSs exhibit enhanced OER catalytic stability compared with the RuRh NSs.

The OER performance of RuRh@(RuRh)O_2 NSs was also investigated in O_2-saturated 1 M KOH as well (Fig. S13†). The overpotentials of RuRh@(RuRh)O_2 NSs and commercial RuO_2 at 10 mA cm^{-2} are 304 mV and 362 mV, and the corresponding Tafel slopes are 80.9 mV dec^{-1} and 165.1 mV dec^{-1}, respectively. Besides, RuRh@(RuRh)O_2 NSs show higher mass activities compared with commercial RuO_2. The above results reveal that the RuRh@(RuRh)O_2 NSs exhibit better OER activity in alkaline media and compared with commercial RuO_2.

We investigate the OER electrocatalysis in the core@shell RuRh@(RuRh)O_2 based on the constructed model through DFT calculations (Fig. 4a). The surface oxidation layer evidentially becomes more electron-rich in RuRh@(RuRh)O_2, which supports the enhanced electron transfer capability (Fig. 4b). In RuRh@(RuRh)O_2, the projected partial density of states (PDOS) shows the modulation of Ru-4d bands, in which the wide covering bands become concentrated with an upshift of the d-band centre.

More importantly, the high electroactivity near the RuRh/RuO_2 interface supports that the close oxide/hydroxide next to the metal substrate is active for the OER especially at low overpotential.[24] The evident alleviation of the e_g–t_{2g} gap on the electrocatalyst surface also demonstrates a smaller energy barrier for electron depletion, which is critical for actualizing efficient OER in the acid and alkaline environment (Fig. 4c). The site-dependent PDOS of O-2p bands displays the crossover of Fermi level (E_F), indicating a high electron transfer capability to facilitate the interaction between the electrocatalyst and the adsorbates (Fig. 4d). Moreover, the free H_2O displays a dominant peak at E_V – 2.5 eV, which highly matches with the Rh-4d bands. Similar well overlapping between the intermediate s,p bands, and the surface RhRu is also noted. This confirms the key role of Rh in facilitating the initial adsorption of H_2O and OH in acidic and alkaline media (Fig. 4e). Further, we analyze the electronic structures in detail regarding the band offset and the e_g–t_{2g} gap. From the core RuRh towards the surface RuO_2 layer, we observe the upshift of Ru 4d-bands from E_V – 2.2 eV to E_V – 1.3 eV. This result supports the substantially enhanced electroactivity due to the formation of the surface oxidation layer (Fig. 4f). Beyond the band offset, the obvious shrink of the gap between the e_g–t_{2g} occurs in the surface oxidation layer. The energy barrier evidentially decreases nearly half the magnitude from the core RuRh of 2.9 eV to 1.4 eV in the shell RuO_2 surface (Fig. 4g). Similarly, the p-bands of O in the surface oxidation layer show the downshift from the surface RuO_2 to the RuRh/RuO_2 interface. Thus, the efficient electron transfer from the catalyst towards adsorbates is achieved by the surface oxidation layer (Fig. 4h). Meanwhile, the high electrical conductivity of the core RuRh paves a way for electron transfer from the electron-rich core towards the electroactive shell RuO_2 surface. The collaborated contribution of RuRh and RuO_2 results in the superior OER performance in acidic and alkaline media.

We also reveal the energy pathway to illustrate the physicochemical reaction trend of the core@shell RuRh@(RuRh)O_2 in both acidic and alkaline OERs. For the acidic OER, the reaction of [*OH + H_2O + H^+ → *O + H_2O + 2H^+] requires the highest energy cost of 1.45 eV at $U = 0$ V, indicating the corresponding overpotential of 0.22 V to achieve the complete downhill trend of the OER process, which is highly consistent with the experimental results (Fig. 4i). Meanwhile, we observe that the reaction [*OH + 3OH^- → *O + 2OH^- + H_2O] is the rate-determining step with an energy barrier of 1.52 eV in the alkaline OER. The final formation of O_2 exhibits a similar barrier height. The corresponding overpotential of 0.29 V for the alkaline OER is in good agreement with the 304 mV overpotential from the experiments (Fig. 4j). There, the highly electroactive shell oxidation layer significantly boosts the electron transfer capability to actualize the superior OER in acidic and alkaline media.

Conclusions

In summary, this work presents a rational design of ultrathin RuRh@(RuRh)O_2 core@shell nanosheets as highly stable and active OER electrocatalysts. The 2D morphology of ultrathin RuRh@(RuRh)O_2 core/shell nanosheets with a high degree of abundant surface atoms serving as active sites guarantees that the high OER activity and the shell structure of RuO_2/RhO_2 oxides could lower the fast Ru dissolution of metallic RuRh NSs during the OER process, revealed by rotating ring disk electrode (RRDE) measurements for simultaneously recording the dissolution of Ru on the ring electrode and the *ex situ* measurement of Ru dissolution using the galvanostatic method. Therefore, the ultrathin RuRh@(RuRh)O_2 core@shell nanosheets exhibit much better OER stability than the metallic RuRh NSs. DFT calculations unravel the superior OER performance based on the electro-activation by the surface oxidation layer. The core RuRh preserves the high electrical conductivity for electron transfer to the surface. The shell RuO_2 layer further pumps the electrons towards the adsorbates to efficiently facilitate the consecutive reactions in the OER. The enhancement of the OER is guaranteed based on the synergistic contribution by the RuRh core and oxidation layer shell. The present work provides a new vision for tuning the ultrathin 2D heterostructures to balance the OER activity and stability.

Conflicts of interest

There are no conflicts to declare.

Acknowledgements

This work was financially supported by the Beijing Natural Science Foundation (No. JQ18005), the "XPLORER PRIZE" (Tencent), the National Natural Science Foundation of China (No. 51671003 and 51672007), the National Key R&D Program of China (No. 2016YFB0100201), the BIC-ESAT project, the China Postdoctoral Science Foundation (No. 2017M610022), the fund of the State Key Laboratory of Solidification Processing in NPU (Grant No. SKLSP202004) and the Young Thousand Talented Program. P. G. acknowledges the support from the Key-Area Research and Development Program of GuangDong Province

(No. 2018B030327001 and 2018B010109009), and the "2011 Program" Peking-Tsinghua-IOP Collaborative Innovation Center for Quantum Matter.

References

1 A. Grimaud, A. Demortière, M. Saubanère, W. Dachraoui, M. Duchamp, M.-L. Doublet and J.-M. Tarascon, *Nat. Energy*, 2016, **2**, 1–10.
2 H. N. Nong, T. Reier, H.-S. Oh, M. Gliech, P. Paciok, T. H. T. Vu, D. Teschner, M. Heggen, V. Petkov and R. Schlögl, *Nat. Catal.*, 2018, **1**, 841–851.
3 L. C. Seitz, C. F. Dickens, K. Nishio, Y. Hikita, J. Montoya, A. Doyle, C. Kirk, A. Vojvodic, H. Y. Hwang and J. K. Norskov, *Science*, 2016, **353**, 1011–1014.
4 J. Shan, C. Guo, Y. Zhu, S. Chen, L. Song, M. Jaroniec, Y. Zheng and S.-Z. Qiao, *Chem*, 2019, **5**, 445–459.
5 J. Feng, F. Lv, W. Zhang, P. Li, K. Wang, C. Yang, B. Wang, Y. Yang, J. Zhou and F. Lin, *Adv. Mater.*, 2017, **29**, 1703798.
6 T. Reier, H. N. Nong, D. Teschner, R. Schlögl and P. Strasser, *Adv. Energy Mater.*, 2017, **7**, 1601275.
7 C. Spoeri, J. T. H. Kwan, A. Bonakdarpour, D. P. Wilkinson and P. Strasser, *Angew. Chem., Int. Ed.*, 2017, **56**, 5994–6021.
8 J. Creus, J. De Tovar, N. Romero, J. García-Antón, K. Philippot, R. Bofill and X. Sala, *ChemSusChem*, 2019, **12**, 2493–2514.
9 R. Forgie, G. Bugosh, K. Neyerlin, Z. Liu and P. Strasser, *Electrochem. Solid State Lett.*, 2010, **13**, B36.
10 S. Cherevko, A. R. Zeradjanin, A. A. Topalov, N. Kulyk, I. Katsounaros and K. J. Mayrhofer, *ChemCatChem*, 2014, **6**, 2219–2223.
11 M. Schalenbach, O. Kasian, M. Ledendecker, F. D. Speck, A. M. Mingers, K. J. Mayrhofer and S. Cherevko, *Electrocatalysis*, 2018, **9**, 153–161.
12 S. Cherevko, S. Geiger, O. Kasian, N. Kulyk, J.-P. Grote, A. Savan, B. R. Shrestha, S. Merzlikin, B. Breitbach and A. Ludwig, *Catal. Today*, 2016, **262**, 170–180.
13 (*a*) S. Cherevko, A. R. Zeradjanin, A. A. Topalov, N. Kulyk, I. Katsounaros and K. J. Mayrhofer, *ChemCatChem*, 2014, **6**, 2219–2223; (*b*) L. Gloag, T. M. Benedetti, S. Cheong, C. E. Marjo, J. J. Gooding and R. D. Tilley, *J. Am. Chem. Soc.*, 2018, **140**, 12760–12764.
14 (*a*) Y. Xing, K. Wang, N. Li, D. Su, W. Wong, B. Huang and S. Guo, *Matter*, 2020, **2**, 1494–1508; (*b*) A. Yin, W. Liu, J. Ke, W. Zhu, J. Gu, Y. Zhang and C. Yan, *J. Am. Chem. Soc.*, 2012, **134**, 20479–20489.
15 K.-P. Bohnen, R. Heid, O. de la Pena Seaman, B. Renker, P. Adelmann and H. Schober, *Phys. Rev. B*, 2007, **75**, 092301.
16 R. Shannon, *Solid State Commun.*, 1968, **6**, 139–143.
17 K. Wang, Y. Qin, F. Lv, M. Li, Q. Liu, F. Lin, J. Feng, C. Yang, P. Gao and S. Guo, *Small Methods*, 2018, **2**, 1700331.
18 D. J. Morgan, *Surf. Interface Anal.*, 2015, **47**, 1072–1079.
19 F. Lv, J. Feng, K. Wang, Z. Dou, W. Zhang, J. Zhou, C. Yang, M. Luo, Y. Yang and Y. Li, *ACS Cent. Sci.*, 2018, **4**, 1244–1252.
20 B. Han, M. Risch, S. Belden, S. Lee, D. Bayer, E. Mutoro and Y. Shao-Horn, *J. Electrochem. Soc.*, 2018, **165**, F813–F820.
21 C. Wei, R. R. Rao, J. Peng, B. Huang, I. E. Stephens, M. Risch, Z. J. Xu and Y. Shao-Horn, *Adv. Mater.*, 2019, **31**, 1806296.
22 N. Danilovic, R. Subbaraman, K.-C. Chang, S. H. Chang, Y. J. Kang, J. Snyder, A. P. Paulikas, D. Strmcnik, Y.-T. Kim and D. Myers, *J. Phys. Chem. Lett.*, 2014, **5**, 2474–2478.
23 Y. Lee, J. Suntivich, K. J. May, E. E. Perry and Y. Shao-Horn, *J. Phys. Chem. Lett.*, 2012, **3**, 399–404.
24 S. Zou, M. S. Burke, M. G. Kast, J. Fan, N. Danilovic and S. W. Boettcher, *Chem. Mater.*, 2015, **27**, 8011–8020.